applied sciences

MDPI

Article

Trend-Constrained DTW for Horizontal Well In-Zone Geosteering with Azimuthal Gamma-Ray Data

Zexi Zhao, Bo Zheng, Shouding Li *, Xiukuo Sun, Guanglin Zhang, Zhaobin Zhang, Hao Huang and Xiao Li

State Key Laboratory of Deep Petroleum Intelligent Exploration and Development, Institute of Geology and Geophysics, Chinese Academy of Sciences, Beijing 100029, China; zhaozexi@mail.iggcas.ac.cn (Z.Z.)
* Correspondence: lsdlyh@mail.iggcas.ac.cn

Abstract

In unconventional horizontal drilling, limited logging measurements pose challenges for accurate in-zone positioning and geosteering. This study proposes an azimuthal gamma-ray trend-constrained dynamic time warping (DTW) method with adaptive significance-threshold updating. The relative responses of upper and lower azimuthal gamma-ray measurements are used to identify stratigraphic movement trends and constrain the DTW endpoint search space. A fixed-start–sliding-end matching strategy estimates the endpoint position using an independently field-interpreted starting position. An XGBoost classifier predicts the significance threshold from window-level features to improve adaptability to varying gamma-ray responses. The predicted endpoint position is further combined with wellbore trajectory information to estimate the local apparent formation dip for auxiliary steering. Leave-one-well-out cross-validation on five model-development wells (247 windows) yielded a well-level macro-averaged mean absolute error (MAE) of 0.332 m relative to field-interpreted reference positions. Independent validation on two additional horizontal wells, H1 and H2, achieved MAEs of 0.314 and 0.338 m, respectively, representing reductions of 12.8% and 13.8% compared with fixed-threshold trend-constrained DTW. Compared with unconstrained DTW, the proposed method reduced the MAE by 55.9% and 44.8% on H1 and H2, respectively. These results demonstrate the potential of combining azimuthal trend constraints with adaptive threshold updating for gamma-ray-based in-zone positioning and support its applicability to previously unseen wells within the investigated geological block.

Keywords: azimuthal gamma-ray; trend-constrained DTW; intra-layer positioning; geosteering; machine learning; real-time application

Check for updates

Academic Editor: Ricardo Castedo Ruiz

Received: 29 September 2026
Revised: 4 November 2026
Accepted: 5 November 2026
Published: 9 November 2026

Copyright: © 2026 by the authors. Licensee MDPI, Basel, Switzerland. This article is an open access article distributed under the terms and conditions of the Creative Commons Attribution (CC BY) license.

1. Introduction

Accurate well placement along horizontal well sections requires advanced technologies, not only to improve well productivity but also to minimize the risk of undesirable downhole events through additional measurements and real-time monitoring. In unconventional oil and gas development, preliminary knowledge of the spatial distribution, thickness variation, and geophysical response characteristics of the target interval can typically be obtained from offset well logs, core analysis, and seismic data. With such prior knowledge, geosteering while drilling involves real-time in-zone positioning and trajectory adjustment informed by existing geological knowledge, rather than operating under completely unknown geological conditions [1,2]. Gamma-ray logging is commonly used to identify organic-rich shale, high-gamma source rocks, and adjacent low-gamma non-productive intervals because of

its relatively low cost, simple implementation, and intuitive interpretation [3,4]. In practice, however, owing to constraints related to tool cost, operational efficiency, and downhole reliability, many production wells are equipped only with gamma-ray-while-drilling or near-bit azimuthal gamma-ray measurements [5,6]. Therefore, achieving reliable in-zone positioning and auxiliary steering under gamma-only measurement conditions remains an important engineering challenge for cost-effective horizontal well development [7,8].

Existing geosteering technologies have primarily developed along two directions. One category of methods relies on multi-parameter logging-while-drilling (LWD) data fusion, comprehensively utilizing resistivity, density, sonic, neutron, and other logging information for formation interpretation, boundary identification, and trajectory optimization [9,10]. This type of method can provide relatively abundant geological constraints, but it places high demands on tool suite, data quality, and interpretation workflow, limiting its application in large-scale, low-cost production wells [11,12]. The other category relies on novel azimuthal logging tools, such as near-bit azimuthal gamma-ray and azimuthal resistivity tools, to enhance the capability of near-bit formation boundary identification and layer-crossing trend assessment [13–15]. Among these, near-bit azimuthal gamma-ray measurements offer advantages such as short sensor-to-bit offset, prompt response, and relatively controllable cost, and have been widely applied in field geosteering [16,17].

However, in scenarios where only gamma-ray or azimuthal gamma-ray measurements are available, the assessment of layer-crossing trends and in-zone position still relies heavily on human expertise, lacking a stable and reproducible real-time quantitative analysis method. To address this, some researchers have recently attempted to introduce Dynamic Time Warping (DTW), a method capable of measuring the morphological similarity between two sequences under nonlinear stretching or compression, which has been applied to tasks such as well log correlation, inter-well stratigraphic correlation, and horizon identification [18,19]. In real-time geosteering, DTW can be used to locally match the current gamma-ray window with the standard type log, so as to estimate the relative in-zone position of the drill bit [20]. However, conventional DTW lacks the directional prior required for geosteering. When the standard type log contains similar shapes or noise, unconstrained DTW matching is prone to mismatching, leading to unstable in-zone positioning.

Azimuthal gamma-ray measurements can separately reflect the gamma-ray responses of the formations above and below the drill bit, and this response sequence encodes the movement trend of the bit relative to the formation (up-cutting, down-cutting, or parallel) [21]. Recent studies [4] have begun to explore the combination of DTW with azimuthal gamma-ray data, but their core focus is on addressing the discrete event detection problem of "whether the drill bit is crossing a formation boundary," rather than the continuous in-zone positioning when the bit is within the target layer. The latter is of more general value in the development of unconventional long horizontal wells, yet remains inadequately addressed. Therefore, determining how to transform the vertical movement trend provided by azimuthal gamma-ray data—a critical prior—into effective constraints on the DTW matching process is a key challenge facing current low-cost geosteering techniques.

To address the above issues, this paper proposes a real-time in-zone geosteering method based on azimuthal gamma-ray trend-constrained Dynamic Time Warping (DTW). Unlike existing DTW-based geosteering methods [4], which focus on detecting the discrete event of whether the drill bit is crossing a formation boundary, the proposed method concentrates on continuous in-zone quantitative positioning when the bit is within the target layer, thus offering a complementary problem formulation. The method takes real-time gamma-ray, upper azimuthal gamma-ray, lower azimuthal gamma-ray, and wellbore trajectory data as input, uses a standard type log established from offset wells or a block-scale geological model as reference, first identifies the vertical movement trend of the drill bit relative to

the formation, then transforms this trend into constraints on the DTW endpoint search space, and constructs a fixed-start–sliding-end trend-constrained DTW matching approach to estimate the relative vertical position of the current window endpoint within the target zone. On this basis, the local apparent formation dip angle is estimated by incorporating the geometric relationship of the wellbore trajectory, and auxiliary steering recommendations are generated. To reduce the impact of fixed empirical thresholds on the stability of trend identification, a key threshold adaptive update module is further constructed. The overall workflow is shown in Figure 1.

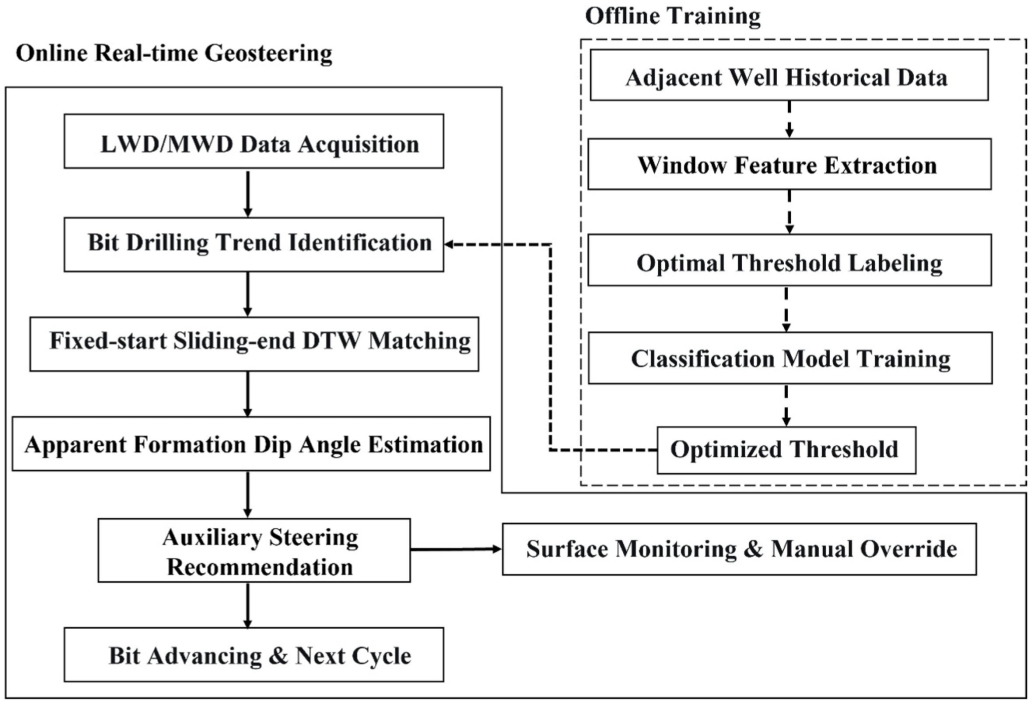

Figure 1. Framework of the trend-constrained DTW geosteering method with adaptive threshold updating.

The five offset wells used for model development (W1–W5) and the two independent field-validation wells (H1 and H2) are located in the Da'an Block of the Sichuan Basin, China, targeting shale gas reservoirs in the Longmaxi Formation. Although all seven wells are located within the same geological block, H2 is geographically farther from the five model-development wells than H1, providing an additional spatially separated validation case. The target interval, primarily comprising organic-rich siliceous shale in the first member of the Longmaxi Formation, is characterized by relatively stable stratigraphic architecture, good lateral continuity, and distinct gamma-ray responses [22–25]. These geological characteristics provide favorable conditions for gamma-ray-based in-zone positioning. Nevertheless, the validation results should be interpreted within the geological conditions investigated in this study, rather than as evidence of general applicability to highly heterogeneous formations or other sedimentary basins.

2. Azimuthal Gamma-Ray Trend-Constrained DTW Geosteering Method

2.1. Azimuthal Gamma-Ray Trend Identification

Azimuthal gamma-ray measurements can separately acquire the gamma-ray responses of the formations above and below the drill bit. For a given formation interface, the upper azimuthal gamma-ray, real-time gamma-ray, and lower azimuthal gamma-ray logs generally exhibit similar log signatures, with the main difference lying in the sequence in which characteristic responses appear. In theory, when the bit is up-cutting relative to the

formation, the upper azimuthal gamma-ray typically responds significantly earlier than the lower; when down-cutting, the opposite happens; and when the bit travels approximately parallel to the formation, the response difference between the two is small [21,26].

Figure 2a illustrates, based on the geometric relationship between the wellbore trajectory and the formation interface, how the vertical movement of the drill bit relative to the formation leads to a difference in the response timing of the upper and lower azimuthal gamma-ray. In the figure, the red and yellow curves represent the change segments of the upper and lower gamma-ray when the bit is drilling upward, respectively. It can be seen that both curves first drop from the starting point to a trough and then rise to the end point. Because the drill bit itself possesses a vertical thickness, the upper gamma-ray reaches the trough earlier than the lower gamma-ray. Figure 2b further verifies this phenomenon through the gamma-ray response curves: the trough of the red curve (upper gamma-ray) appears at a smaller matching index, while the trough of the yellow curve (lower gamma-ray) appears later. So the vertical direction of movement can be obtained by comparing the curve shapes of gamma rays in the same window. Figure 3 illustrates the schematic relationship of the azimuthal gamma-ray response sequences under three typical layer-crossing modes. Figure 3a shows a typical up-cutting case, and the real-time gamma-ray log reveals the overall variation trend within this window: the highest peak appears first, followed by a decline to a trough and then a rise. Therefore, the upper and lower azimuthal gamma-ray responses should also exhibit a peak followed by a trough within this window, and the upper azimuthal gamma-ray peak appears earlier, indicating that the drill bit is up-cutting at this time.

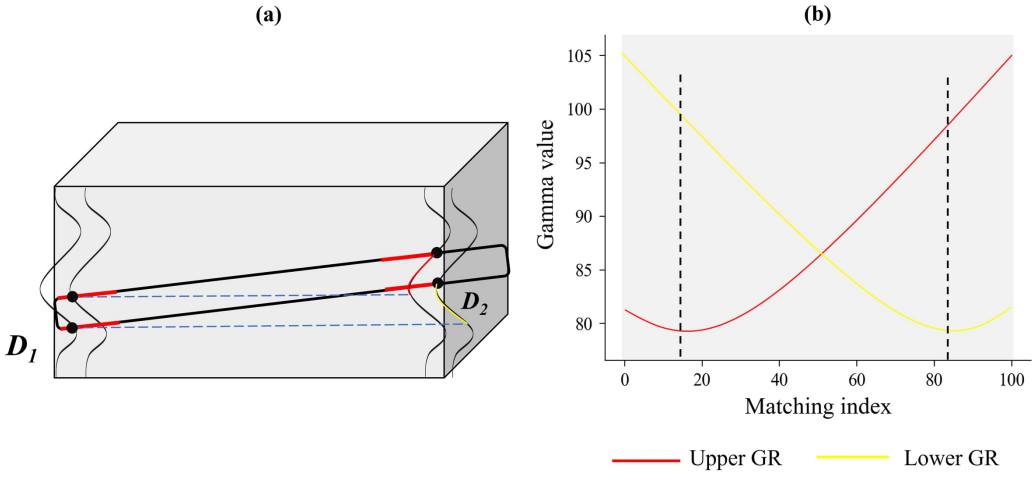

Figure 2. Geometric origin and curve characteristics of azimuthal gamma-ray responses during up-cutting. (**a**) Geometric relationship between wellbore trajectory and formation interface; (**b**) comparison of upper and lower azimuthal gamma-ray response curves.

In this study, an analysis window refers to a segment of logging data defined by measured depth (MD), rather than elapsed time. The field-validation windows generally span 20–40 m, corresponding to the geosteering decision intervals used in field operations. Let the upper and lower azimuthal gamma-ray sequences within the i-th window be defined as:

$$G_{u,i} = \{g_{u,i}(k)\}_{k=1}^{n}, G_{d,i} = \{g_{d,i}(k)\}_{k=1}^{n} \quad (1)$$

where $g_{u,i}(k)$ and $g_{d,i}(k)$ denote the measured values of the upper and lower azimuthal gamma-rays at the k-th sampling point, respectively. To reduce the impact of noise on feature point identification, the upper and lower azimuthal gamma-ray curves are first smoothed [27,28], with the smoothed sequences denoted as $\tilde{g}_{u,i}(k)$ and $\tilde{g}_{d,i}(k)$.

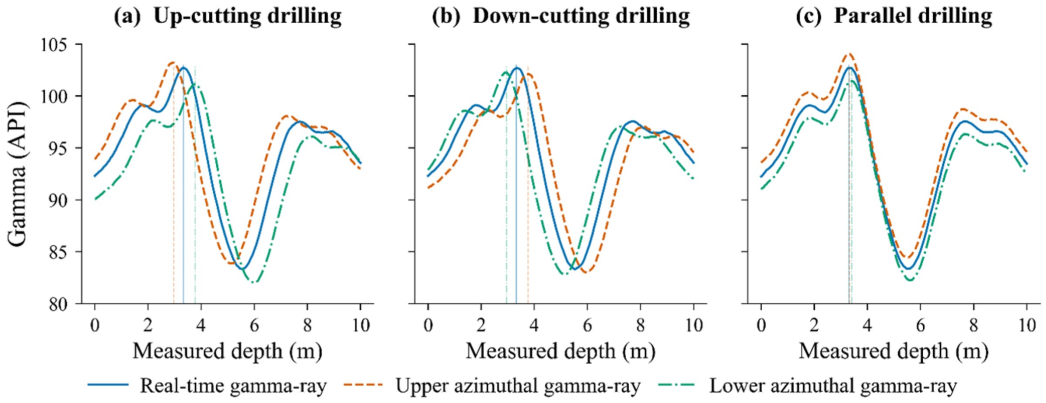

Figure 3. Schematic illustration of azimuthal gamma-ray trend identification based on the relative response order of the upper azimuthal gamma-ray, real-time gamma-ray, and lower azimuthal gamma-ray curves under upcut, downcut, and parallel drilling conditions.

Within the current window, the primary response positions of the upper and lower azimuthal gamma-ray curves are defined as:

$$\tau_{u,i} = \underset{k}{\operatorname{argmax}} \left| \tilde{g}_{u,i}(k) - \overline{g}_{u,i} \right|, \tau_{d,i} = \underset{k}{\operatorname{argmax}} \left| \tilde{g}_{d,i}(k) - \overline{g}_{d,i} \right| \tag{2}$$

where $\overline{g}_{u,i}$ and $\overline{g}_{d,i}$ denote the window means of the smoothed upper and lower azimuthal gamma-ray sequences, respectively, and $\tau_{u,i}$ and $\tau_{d,i}$ denote the sampling indices at which the corresponding smoothed curves exhibit their maximum absolute deviations from these means. This criterion identifies the most pronounced deviation within each window without explicitly detecting local peaks or troughs. The difference between the two indices is subsequently used to characterize the relative response order of the upper and lower azimuthal gamma-ray measurements.

When the maximum absolute deviation of either curve is below the prescribed significance threshold, the corresponding response is regarded as insufficiently distinctive for reliable trend identification. In this case, the trend is assigned to the parallel/unknown category, and a conservative endpoint search range is used in the subsequent DTW matching process to reduce the risk of imposing an incorrect directional constraint.

When multiple sampling points exhibit the same maximum absolute deviation, the earliest sampling position is selected to ensure a unique response index.

The relative response order of the upper and lower azimuthal gamma-ray curves is quantified by the difference between their dominant response indices:

$$\Delta\tau_i = \tau_{u,i} - \tau_{d,i} \tag{3}$$

The vertical movement trend of the drill bit, T_i, can then be determined as:

$$T_i = \begin{cases} \text{up-cutting}, & \Delta\tau_i < -\varepsilon_\tau \\ \text{down-cutting}, & \Delta\tau_i > \varepsilon_\tau \\ \text{parallel/unknown}, & |\Delta\tau_i| \le \varepsilon_\tau \end{cases} \tag{4}$$

where ε_τ is a non-negative tolerance threshold for the response index difference, expressed in sampling intervals. It distinguishes meaningful differences in the dominant response positions of the upper and lower azimuthal gamma-ray curves from minor deviations potentially caused by noise. When $|\Delta\tau_i| \le \varepsilon_\tau$, the trend is classified as parallel/unknown, and a conservative bidirectional search strategy is adopted in the subsequent DTW matching process to avoid imposing an unreliable directional constraint.

2.2. Trend-Constrained DTW Matching

After determining the vertical movement trend of the drill bit, it is necessary to further match the current real-time gamma-ray window with the standard-type log to determine the relative position of the current window endpoint within the target zone. Let the real-time gamma-ray sequence of the i-th window be:

$$R_i = \{r_i(k)\}_{k=1}^{n} \tag{5}$$

and the standard type log be denoted as:

$$S(z), z \in [z_{\min}, z_{\max}] \tag{6}$$

where z represents the vertical coordinate along the standard-type log, which can be interpreted as the vertical distance from the top boundary of the target zone.

This paper adopts a fixed-start–sliding-end DTW matching strategy. For the i-th analysis window, let the starting stratigraphic position independently interpreted by the field geosteering engineer be denoted by $\hat{z}_{i-1}$, let z_e denote a candidate endpoint position, and let Δz_{max} represent the maximum allowable vertical search distance. Based on the identified azimuthal gamma-ray trend, the candidate endpoint search space is defined as follows:

$$\Omega_i = \begin{cases} [\hat{z}_{i-1} - \Delta z_{max}, \hat{z}_{i-1}], T_i = \text{upcut} \\ [\hat{z}_{i-1}, \hat{z}_{i-1} + \Delta z_{max}], T_i = \text{downcut} \\ [\hat{z}_{i-1} - \Delta z_{max}, \hat{z}_{i-1} + \Delta z_{max}], T_i = \text{parallel/unknown} \end{cases} \tag{7}$$

It should be noted that the trend constraint proposed in this paper is fundamentally different from traditional DTW path constraints [29–31]. These traditional constraints restrict the degree of warping of the matching path along the time axis, whereas the proposed method uses the azimuthal gamma-ray trend to constrain the candidate endpoint search space—that is, it reduces the involvement of standard log segments whose direction is inconsistent with the bit's movement direction in the matching process, without altering the internal path boundary conditions of DTW. This directional prior guidance leverages the known characteristic of the bit's movement direction in geosteering—a geological prior that conventional time series matching methods do not possess.

For any candidate endpoint $z_e \in \Omega_i$, a standard log segment $S_i(z_e)$, extending from the independently field-interpreted starting stratigraphic position $\hat{z}_{i-1}$ to the candidate endpoint z_e, is extracted from the standard-type log. The DTW distance between this segment and the real-time gamma-ray window R_i is then calculated as follows:

$$D(R_i, S_i) = \min_{\pi} \sum_{(p,q)\in\pi} [r_i(p) - s_i(q)]^2 \tag{8}$$

where π is the DTW matching path satisfying the boundary, continuity, and monotonicity constraints, and p and q are the sampling point indices in the real-time gamma-ray sequence and the standard log segment, respectively.

Finally, the candidate endpoint with the minimum DTW distance is selected as the endpoint position of the current window:

$$\hat{z}_i = \arg\min_{z_e \in \Omega_i} D(R_i, S_i(z_e)) \tag{9}$$

where $\hat{z}_i$ is the vertical position of the predicted endpoint of the current window within the standard-type log. In the present field implementation, the starting stratigraphic position of each analysis window is independently determined from the field geosteering engineer's interpretation and is used as a fixed matching anchor. The proposed algorithm estimates

the endpoint position within the geologically constrained search range. Importantly, the predicted endpoint of the preceding window is not automatically transferred to the next window as its starting position. Thus, the fixed-start–sliding-end strategy refers to the matching operation within an individual analysis window rather than recursive positioning across successive windows. Compared with conventional bidirectional search DTW, the proposed method formulates the azimuthal gamma-ray trend information as a candidate endpoint search constraint, so that the curve matching is governed not only by the morphological similarity of the gamma-ray logs but also by the prior constraint of the bit's vertical movement direction. Figure 4 illustrates the schematic of the fixed-start–sliding-end trend-constrained DTW matching process.

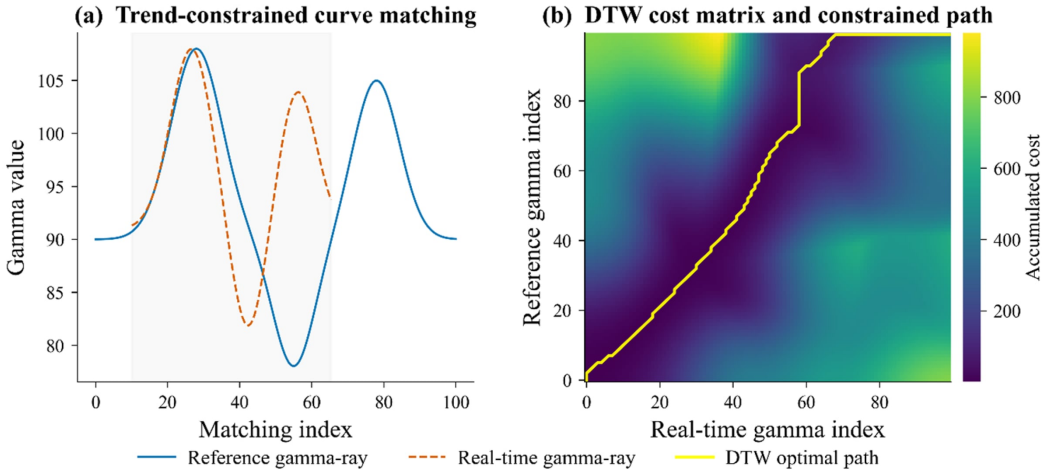

Figure 4. Fixed-start sliding-end DTW matching constrained by azimuthal gamma trend. (**a**) Schematic of curve matching between real-time gamma and standard template gamma. (**b**) DTW cost matrix and the constrained optimal path.

2.3. Apparent Formation Dip Angle Estimation

After obtaining the predicted endpoint position of the current analysis window using trend-constrained DTW, the local apparent formation dip angle can be estimated by combining the independently interpreted starting position, the predicted endpoint position, and the wellbore trajectory geometry. The calculation is performed within the current analysis window and does not require the predicted endpoint of the preceding window.

Let D_1 denote the starting point of the current analysis window, whose stratigraphic position is independently interpreted by the field geosteering engineer, and let D_2 denote the endpoint of the same window, whose stratigraphic position is predicted using the proposed trend-constrained DTW method. The horizontal displacement between D_1 and D_2 is denoted by Δl_d, and the corresponding change in true vertical depth of the wellbore trajectory is denoted by ΔTVD.

The vertical distances from the wellbore to the top boundary of the target zone D_1 and D_2 are denoted by Δh_1 and Δh_2, respectively. The starting-point distance Δh_1 is determined from the field-interpreted stratigraphic position, whereas the endpoint distance Δh_2 is obtained from the proposed DTW-based positioning result. Based on the geometric relationship illustrated in Figure 5, the local apparent formation dip angle α_2 is calculated as follows:

$$\alpha_2 = \arctan\left(\frac{\Delta h_d}{\Delta l_d}\right) = \arctan\left(\frac{\Delta TVD - (\Delta h_2 - \Delta h_1)}{\Delta l_d}\right) \quad (10)$$

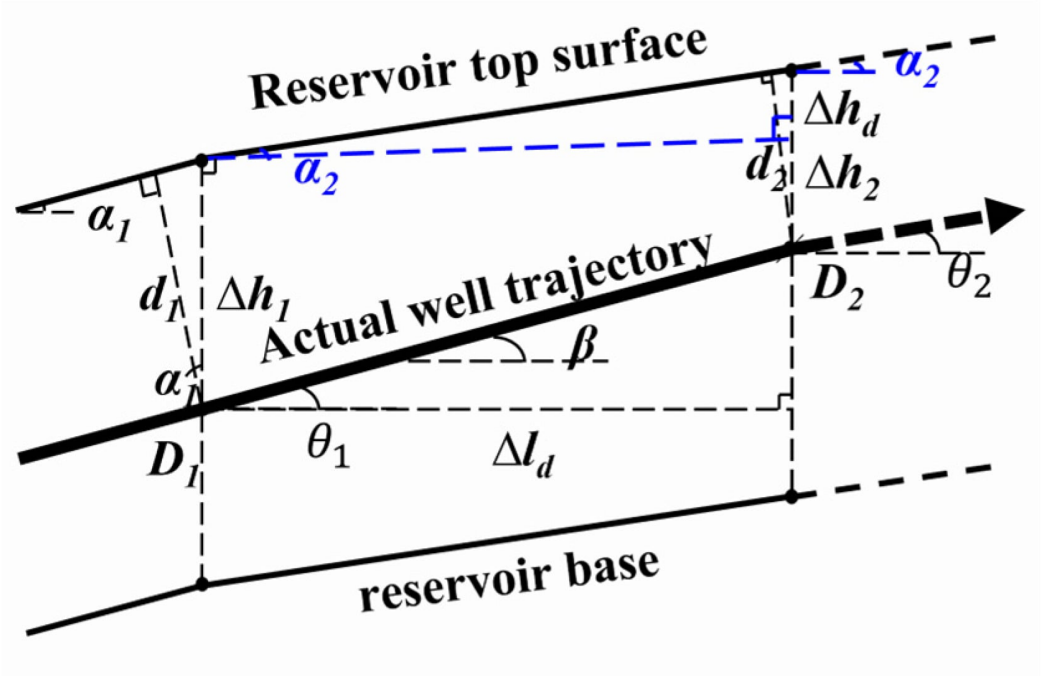

Figure 5. Schematic diagram for apparent formation dip angle calculation.

The estimated angle α_2 represents the local apparent formation dip over the current analysis window. The calculation uses the independently interpreted starting position and the predicted endpoint position of the same window, without relying on the predicted endpoint of the preceding window.

2.4. Auxiliary Steering Recommendation Generation

After obtaining the current window endpoint position and the local apparent formation dip angle, auxiliary steering recommendations can be further generated. Let the thickness of the target zone be H, and let the vertical distance from the current window endpoint to the top boundary of the target zone be d_i:

$$d_i = \hat{z}_i \tag{11}$$

Then, the position state P_i of the drill bit relative to the target zone can be classified as:

$$P_i = \begin{cases} \text{abovetarget}, d_i < 0 \\ \text{insidetarget}, 0 \le d_i \le H \\ \text{belowtarget}, d_i > H \end{cases} \tag{12}$$

To distinguish the inner safe region of the target zone from the near-boundary risk regions, let the boundary safety distance be δ. If $0 \le d_i \le \delta$, the bit is considered to be approaching the top boundary of the target zone; if $H - \delta < d_i \le H$, it is approaching the bottom boundary; and if $\delta \le d_i \le H - \delta$, it is located in the middle of the target zone.

The angular difference between the wellbore trajectory inclination $\theta_{b,i}$ and the local apparent formation dip angle α_2 is further defined as:

$$\Delta\theta_i = \theta_{b,i} - \hat{\theta}_{f,i} \tag{13}$$

where $\theta_{b,i}$ is the wellbore trajectory inclination of the current window (positive when inclining upward along the wellbore trajectory profile). When $\Delta\theta_i > 0$, it indicates that the wellbore trajectory inclination is greater than the apparent formation dip angle, and the bit has an up-cutting trend relative to the formation; when $\Delta\theta_i < 0$, it indicates that the

wellbore trajectory inclination is less than the apparent formation dip angle, and the bit has a down-cutting trend; and when $\Delta\theta_i$ is close to zero, the bit is traveling approximately parallel to the formation.

Based on the bit position relative to the target zone P_i and the angular difference $\Delta\theta_i$, auxiliary steering recommendation rules can be formulated as shown in Table 1.

Table 1. Auxiliary steering recommendations based on bit position and angular difference states.

Bit Position State	$\Delta\theta_i > 0$ (Up-Cutting)	$\Delta\theta_i \approx 0$ (Parallel)	$\Delta\theta_i < 0$ (Down-Cutting)
Middle of target zone	Hold Inclination	Hold Inclination	Hold Inclination
Approaching top boundary	Decrease Inclination	Decrease Inclination (Monitor)	Hold Inclination (Monitor)
Approaching bottom boundary	Hold Inclination (Monitor)	Increase Inclination (Monitor)	Increase Inclination
Above top boundary	Decrease Inclination	Decrease Inclination	Decrease Inclination
Below bottom boundary	Increase Inclination	Increase Inclination	Increase Inclination

In Table 1, "Hold inclination" means maintaining the current wellbore trajectory trend; "Increase inclination" means recommending an increase in wellbore trajectory inclination to steer the bit back toward the upper part of the target zone; "Decrease inclination" means recommending a decrease in wellbore trajectory inclination to steer the bit back toward the lower part of the target zone; and "Monitor" means that the current state has not yet reached a mandatory adjustment condition, but the bit is approaching the boundary of the target zone or the angular difference exhibits a sustained increasing trend, and further judgment should be made in conjunction with subsequent window results.

It should be noted that the outputs of this paper are auxiliary steering recommendations, rather than automatic closed-loop control commands. Actual trajectory adjustment still requires comprehensive consideration of the build-up rate limit of near-bit tools, wellbore trajectory smoothness, engineering safety constraints, and the empirical judgment of field geosteering engineers.

3. Sensitivity Analysis and Adaptive Updating of Key Thresholds

Section 2 established a real-time geosteering method based on azimuthal gamma-ray trend identification and trend-constrained DTW matching. The matching performance of this method depends on a set of empirical parameters, among which the trend identification threshold directly affects the extraction of azimuthal gamma-ray response points and further influences the DTW candidate endpoint search space. If this threshold remains a fixed empirical value over an extended interval, trend misidentification or constraint failure may occur when the gamma-ray response intensity, noise level, or azimuthal gamma-ray difference varies along the wellbore section.

To reduce the impact of fixed empirical thresholds on algorithm stability, this paper constructs a key threshold adaptive update module. This module does not alter the core algorithm structure of Section 2; instead, it learns the relationship between window state features and the optimal threshold from offset well historical data in the offline phase [32],

and dynamically adjusts the trend identification significance threshold according to current window features in the online phase [33].

3.1. Sensitivity Analysis of Key Parameters

The algorithm presented in Section 2 involves multiple components, including trend identification, DTW matching, dip angle estimation, and steering recommendations, and different parameters affect the positioning error to varying degrees. Jointly optimizing all parameters directly would not only increase model complexity, but also easily lead to overfitting given the limited sample size. Therefore, this paper first conducts a parameter sensitivity analysis using the controlled variable method and grid search.

The mean absolute endpoint positioning error across N analysis windows is defined as:

$$\mathrm{MAE}(\lambda) = \frac{1}{N}\sum_{i=1}^{N}\left|\hat{z}_i(\lambda_s) - z_i^{\mathrm{ref}}\right| \tag{14}$$

To quantify the influence of different algorithm parameters on positioning accuracy, the mean absolute endpoint positioning error (MAE) across the analysis windows is adopted as the evaluation metric, as defined in Equation (14). Here, N denotes the number of analysis windows, λ represents the parameter under investigation, and $\hat{z}_i(\lambda)$ and z_i^{ref} denote the predicted and field-interpreted reference endpoint positions of the i-th window, respectively. During the sensitivity analysis, each parameter is varied over its predefined range while the remaining parameters are held constant.

The results of the parameter sensitivity analysis are presented in Figure 6. Figure 6a ranks the candidate parameters according to their influence on positioning accuracy, quantified by the difference between the maximum and minimum mean absolute errors within the investigated parameter ranges. The maximum search distance exhibits the highest sensitivity, followed by the monotonic total threshold, whereas parameters such as the DTW recalculation threshold have relatively limited effects on positioning accuracy.

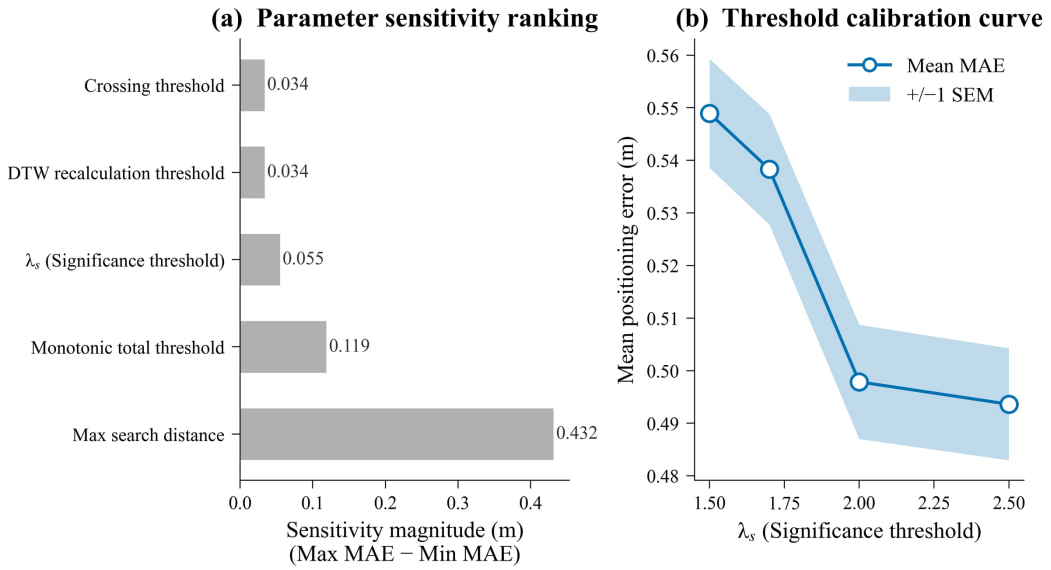

Figure 6. Parameter sensitivity analysis and significance threshold calibration. (**a**) Sensitivity ranking of key parameters and (**b**) calibration curve for the significance threshold.

Although the maximum search distance and monotonic total threshold show greater sensitivity, they primarily control the geometric search range and the admissible matching behavior, respectively. Their selection must therefore account for the geological characteristics of the target interval and the stability of the matching procedure. In the present

implementation, these parameters are retained as fixed settings rather than being included in the online adaptive updating module.

In contrast, Figure 6b illustrates the response of positioning error to changes in the trend identification significance threshold (λ_s). As the threshold increases, the mean positioning error initially decreases and subsequently approaches a relatively stable level. This behavior indicates that threshold selection affects the balance between sensitivity to gamma-ray response features and suppression of weak fluctuations. Because the characteristics of gamma-ray responses may vary among analysis windows, the significance threshold is selected as the target parameter for adaptive updating. The construction of window-specific threshold labels and the corresponding prediction model are described in the following sections.

3.2. Window Feature and Optimal Threshold Label Construction

To enable adaptive prediction of the significance threshold, each analysis window must be represented as a state feature vector. Let the feature vector of the i-th window be:

$$\mathbf{x}_i = \left[x_{i,1}, x_{i,2}, \ldots, x_{i,m}\right] \tag{15}$$

This paper constructs window features from four categories of information: real-time gamma-ray statistical features, azimuthal gamma-ray difference features, curve morphology features, and DTW matching quality features. Their physical meanings are shown in Table 2.

Table 2. Input features of the current window state.

Feature Category	Representative Features	Physical Meaning
Real-time gamma-ray statistical features	Mean (mu_G), standard deviation (sigma_G), range (R_G), skewness (skew), kurtosis (kurt)	Characterize the formation radioactivity level and curve fluctuation characteristics
Azimuthal gamma-ray difference features	Difference mean (diff_mu), difference standard deviation (diff_sigma), difference range (diff_R), difference slope (diff_slope)	Characterize the response difference between the upper and lower azimuthal sectors and the movement trend
Curve morphology features	Number of extreme points (n_peaks, n_valleys), consistency of derivative sign (consistency)	Characterize the local morphological complexity and monotonicity
Matching quality features	Minimum DTW distance (dtw_dist), vertical matching path length (window_len, m)	Characterize the matching difficulty between the real-time curve and the standard curve

In the offline training phase, the optimal significance threshold is determined separately for each historical analysis window through grid search. Four candidate significance thresholds (λ_s in {1.5, 1.7, 1.9, 2.1}) are evaluated while all other algorithm parameters are held constant. For each candidate threshold, trend identification and trend-constrained DTW matching are performed, and the absolute endpoint positioning error is calculated relative to the field-interpreted reference position. The threshold yielding the minimum

error is selected as the training label, as defined in Equation (16). If multiple thresholds yield the same minimum error, the smallest threshold is selected.

$$\lambda_i^* = \arg\min_{\lambda_s \in \Lambda} L_i\left(\hat{z}_i(\lambda_s) - z_i^{\mathrm{ref}}\right) \tag{16}$$

The resulting optimal significance threshold is used as the supervised learning target associated with the feature vector of each historical window. During offline training, the reference endpoint positions are used exclusively to generate threshold labels and evaluate positioning errors. During online application, the trained model predicts the significance threshold from the current window features without requiring the reference endpoint position. All other algorithm parameters remain fixed during threshold prediction and subsequent positioning.

$$\mathcal{D} = \{(\mathbf{x}_i, \lambda_i^*)\}_{i=1}^{N} \tag{17}$$

A total of 247 valid analysis windows were collected from five offset wells (W1–W5) for adaptive threshold model development. The numbers of windows from W1 to W5 were 52, 48, 44, 57, and 46, respectively. To evaluate the model's generalization performance across wells and reduce potential information leakage caused by correlations among windows from the same well, leave-one-well-out (LOWO) cross-validation was introduced. In each fold, four wells were used for model training, while the remaining well was reserved exclusively for testing. This procedure was repeated five times so that each well served once as an independent test well.

The original random window-level partitioning was retained only as an initial assessment of threshold classification performance. Cross-well generalization was evaluated primarily using the LOWO results. The two additional field wells, H1 and H2, were excluded from the model development dataset and reserved for independent field validation.

3.3. Threshold Classification Model Construction and Evaluation

Because the grid-search-derived optimal significance thresholds belong to a predefined discrete candidate set, threshold prediction was formulated as a classification task rather than continuous regression. As shown in Figure 7, preliminary regression predictions clustered within a narrow range and did not adequately capture the discrete label variation. Equation (18) defines the mapping from window features to threshold categories.

$$\hat{c}_i = f(\mathbf{x}_i), \hat{c}_i \in \{1, 2, \ldots, K\} \tag{18}$$

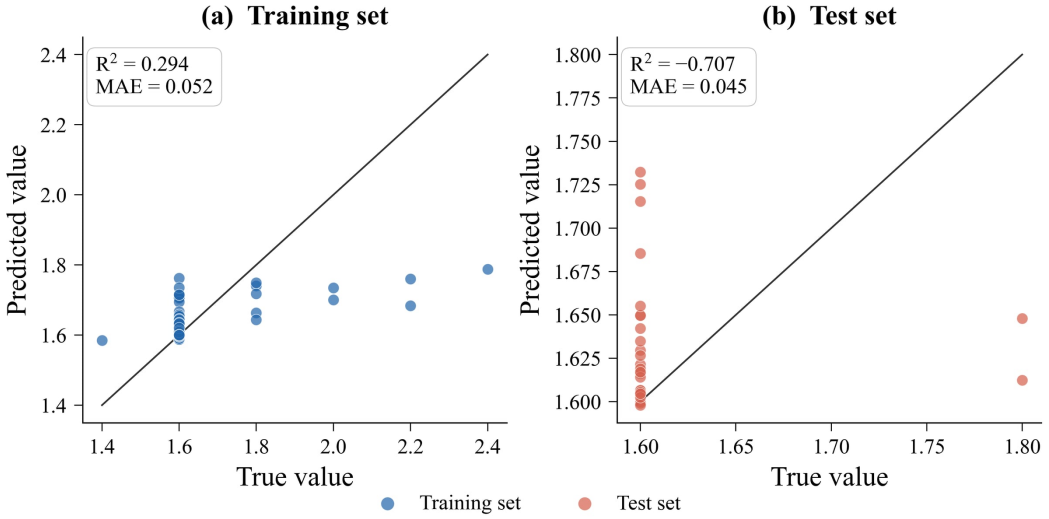

Figure 7. Scatter plots comparing the predicted values and true values of the regression model: (**a**) training set; (**b**) test set.

An XGBoost classifier predicts the threshold category from the window features in Table 2. The predicted category is mapped to its significance threshold for trend identification and DTW endpoint positioning; all other parameters remain fixed.

The input feature 'dtw_dist' is obtained from preliminary DTW matching before XGBoost threshold prediction, using fixed matching settings independent of the predicted threshold. The preliminary matching cost is calculated without using the field-interpreted reference endpoint, thereby avoiding circular dependence and reference-label leakage.

Figure 8 identifies diff_R, mu_G, skew, and preliminary dtw_dist as influential classification features, indicating that azimuthal response differences, gamma-ray statistics, and matching quality contribute to threshold selection.

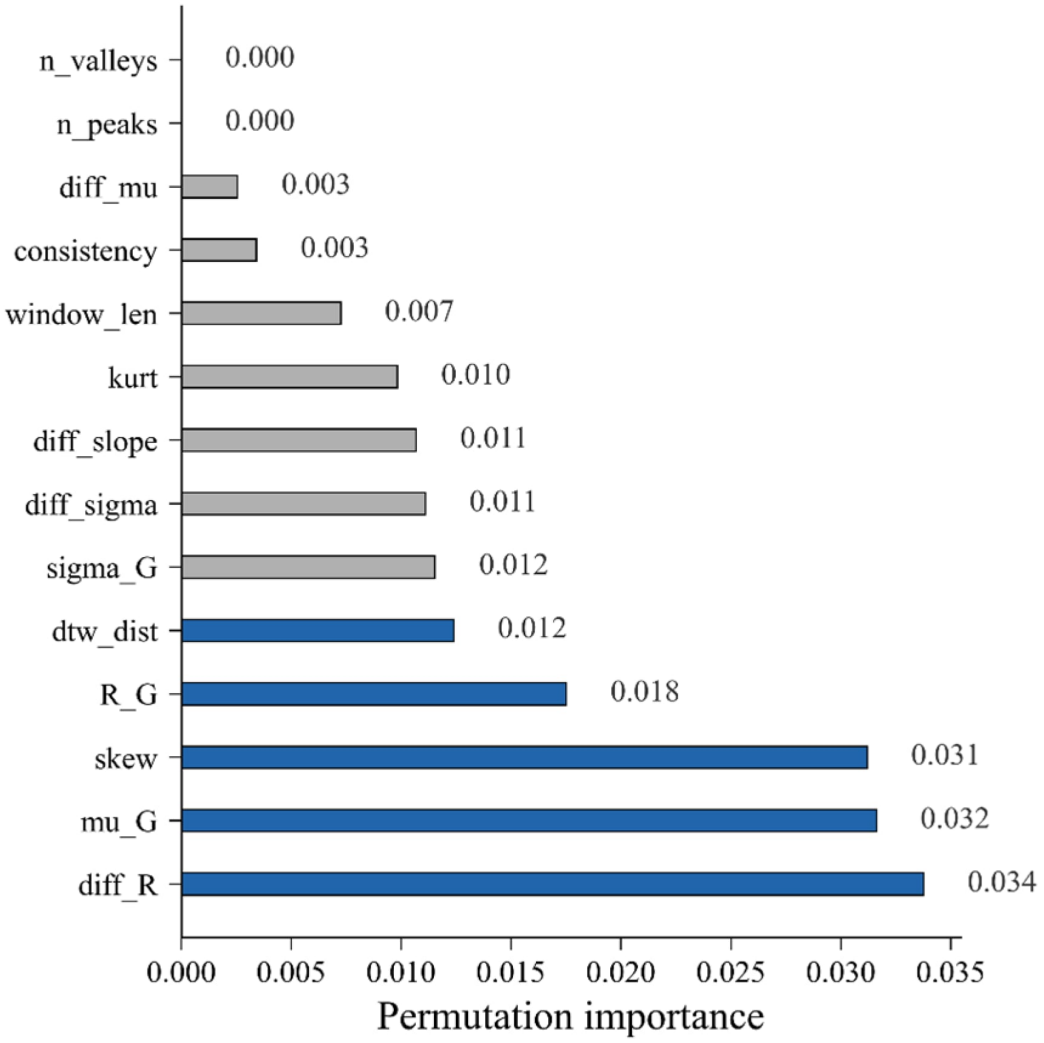

Figure 8. Feature importance ranking of the gradient boosting tree classification model.

Cross-well positioning performance was evaluated using the LOWO protocol described in Section 3.2, with results reported in Table 3.

Table 3 shows that held-out-well MAE ranged from 0.285 to 0.425 m (well-level macro-average: 0.332 m). The proportion of windows with errors ≤0.3 m ranged from 50.0% to 80.4% (macro-average: 69.1%). Each well contributed equally to the macro-average.

These results support within-block cross-well applicability, although performance varies among wells. The separate contribution of adaptive updating is assessed against fixed thresholds in Section 4.

Table 3. Cross-well positioning performance under leave-one-well-out cross-validation.

Test Well	Windows	MAE (m)	Max Error (m)	Error ≤ 0.3 m (%)
W1	52	0.298	0.82	76.9
W2	48	0.341	1.05	64.6
W3	44	0.425	1.47	50.0
W4	57	0.309	0.91	73.7
W5	46	0.285	0.74	80.4
Macro-average	-	0.332	-	69.1

3.4. Online Threshold Update Strategy

After offline model training, the threshold category can be predicted based on current window features during real-time geosteering. For the i-th real-time window, the predicted category $\hat{c}_i$ is obtained from the input feature vector $\mathbf{x}_i$ using Equation (18). Based on a threshold category lookup table, the corresponding predicted threshold value can be obtained as:

$$\hat{\lambda}_{s,i} = Q(\hat{c}_i) \tag{19}$$

where $Q(\cdot)$ denotes the mapping function from category to threshold value. To avoid frequent threshold fluctuations between adjacent windows, exponential smoothing is applied to obtain the significance threshold actually used for the current window:

$$\lambda_{s,i} = \rho\lambda_{s,i-1} + (1-\rho)\hat{\lambda}_{s,i} \tag{20}$$

where $\rho \in [0,1]$ is the smoothing coefficient. The updated threshold is then input into the azimuthal gamma-ray trend identification module in Section 2, and further influences the candidate endpoint search space of the trend-constrained DTW. It should be emphasized that the temporal smoothing described above applies only to the significance threshold. It does not imply recursive updating of the starting stratigraphic position. Each analysis window retains its independently interpreted starting anchor, while the predicted threshold is used to determine the trend constraint for endpoint matching.

It should be noted that the true positioning error is usually not directly accessible during real-time drilling; therefore, the online phase does not use the true error as immediate feedback, but instead relies primarily on metrics such as DTW matching distance, trend identification stability, and positioning continuity between adjacent windows for quality control. When field interpretation results or post-drilling calibration results become available, they can be added to the sample library as delayed feedback for subsequent model updating.

In summary, Section 3 forms a complete technical workflow of "sensitivity analysis—feature construction—threshold label generation—classification prediction—online smoothing update". As an auxiliary module to the core algorithm in Section 2, this module can reduce the risk of failure of a fixed empirical threshold in local well intervals.

4. Field Well Validation and Ablation Analysis

Two independent horizontal wells, H1 and H2, were used to evaluate the positioning performance of the proposed method. Five comparison schemes (A–E) were employed to assess the contributions of trend constraints, adaptive threshold updating, and DTW alignment.

4.1. Data Source and Experimental Setup

Wells H1 and H2 were excluded from model development and evaluated using their respective standard gamma-ray reference logs. H2 is located farther from the five model-

development wells than H1, providing an additional spatially separated validation case within the Da'an Block.

Analysis windows were defined according to field geosteering decision intervals, generally ranging from 20 to 40 m in measured depth. Each window had an independently interpreted starting position and a reference endpoint position provided by field engineers. Only windows with available interpretation benchmarks were evaluated. Thus, the window lengths reflect field practice rather than an experimentally optimized range.

H1 and H2 were evaluated using the same positioning procedure and error metrics. H2 comprised 77 valid windows, and its data were not used for model retraining. The reference endpoint positions for both wells were derived from field interpretations and therefore represent engineering benchmarks rather than independently verified geological ground truth.

Because intervals with severe geological or measurement abnormalities were excluded from the H1 evaluation, the results primarily reflect performance under conventionally interpretable field conditions.

The data provided by test well H1 include: upper and lower azimuthal gamma-ray logs, real-time gamma-ray log, wellbore trajectory data, and the standard-type log of the block. The formation model and the upper and lower azimuthal gamma-ray responses of the horizontal section in Well H1 are shown in Figure 9: the upper left panel displays the upper and lower azimuthal gamma-ray logs (blue and red) varying with measured depth, with their relative response sequence reflecting the vertical movement trend of the drill bit; the lower left panel presents the formation model, showing the target reservoir (purple fill) and the wellbore trajectory (black curve); the right panel shows the standard gamma-ray reference log, serving as the positioning benchmark for the real-time logs and the geological model.

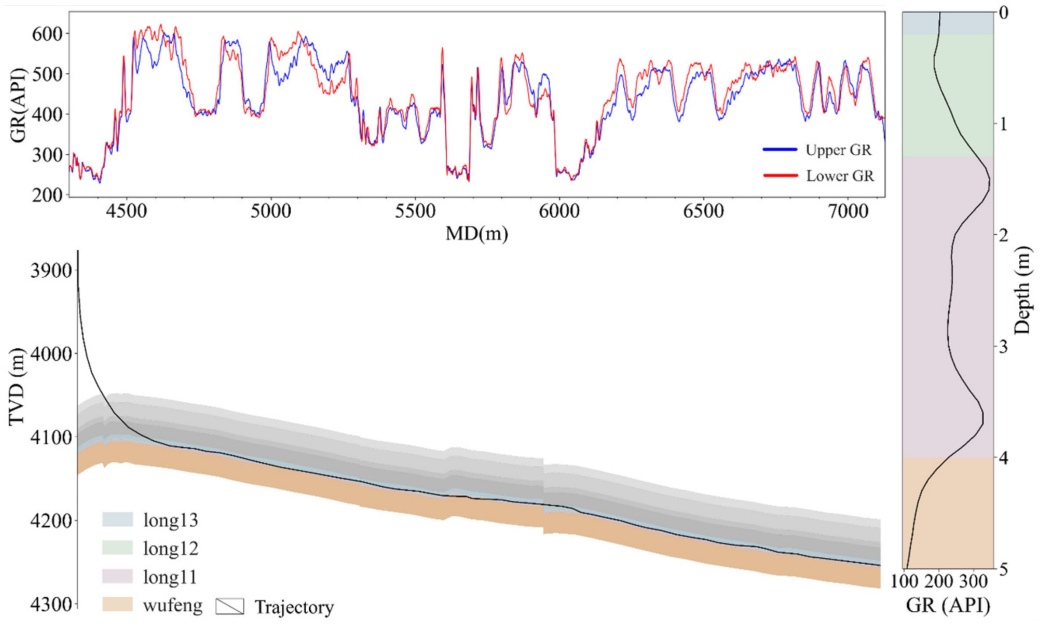

Figure 9. Formation model and gamma-ray responses of the horizontal section in Well H1. (**Upper left**) Upper and lower azimuthal gamma-ray logs; (**Lower left**) formation model showing different stratigraphic units with distinct color fills and wellbore trajectory; (**Right**) standard gamma-ray reference log.

4.2. Comparison Schemes and Evaluation Metrics

To isolate and evaluate the contributions of the trend-constrained DTW matching, the nonlinear alignment capability of DTW, and the threshold adaptive update module, five comparison schemes are designed, covering three key variables: trend constraint (with/without), similarity measure (DTW/Euclidean distance), and threshold strategy (adaptive/fixed-optimal/fixed-suboptimal):

Scheme A: Proposed method. It integrates the trend-constrained DTW matching and the threshold adaptive update module, predicting the significance threshold based on window state features during online processing for azimuthal gamma-ray trend identification and the DTW candidate endpoint search constraint.

Scheme B: Trend-constrained DTW with fixed threshold. It only uses trend-constrained DTW matching, with the core parameters fixed to the most frequent empirical parameter combination in the training set, to evaluate the positioning performance of the trend constraint module under a fixed threshold.

Scheme C: Trend-constrained DTW with deliberately suboptimal threshold. Under the fixed threshold framework of Scheme B, the significance threshold is set to a fixed value outside the optimal range, to simulate performance degradation caused by improper empirical threshold setting.

Scheme D: Unconstrained DTW. It adopts the traditional bidirectional global-search DTW matching without using azimuthal gamma-ray difference information to constrain the candidate endpoint search space, serving as a baseline model to evaluate the contribution of the trend constraint.

Scheme E: Euclidean distance matching. Both the real-time gamma-ray window and the standard log segment are resampled to the same number of points (n = 30) via linear interpolation, and the pointwise Euclidean distance is directly calculated as the similarity measure, without DTW nonlinear path warping, azimuthal trend constraint, or adaptive threshold. This scheme is used to evaluate the performance of a curve matching method without temporal warping capability in real-time gamma-ray geosteering.

This paper adopts the mean absolute positioning error (MAE) as the primary evaluation metric:

$$MAE = \frac{1}{N}\sum_{i=1}^{N}\left|\hat{z}_i - z_i^{ref}\right| \tag{21}$$

where $\hat{z}_i$ is the predicted endpoint position for the i-th window, z_i^{ref} is the field-interpreted reference position, and N is the number of test windows. Auxiliary metrics include the maximum positioning error and the error standard deviation, used to evaluate the stability of the algorithm output.

The positioning performance was evaluated using the mean absolute error (MAE), maximum absolute error, and standard deviation of the window-level positioning errors. For each scheme, the relative reduction in MAE was calculated with respect to Scheme D (unconstrained DTW), which served as the common baseline. A positive reduction indicates improved positioning accuracy, whereas a negative value indicates increased positioning error. The same evaluation criteria were applied to both independent validation wells.

4.3. Ablation Experiment Results

Before quantitatively comparing the matching accuracy of the five schemes, Figure 10 exemplifies the differences among three representative schemes (A, D, and E) using a typical geological window. Figure 10a shows the upper and lower azimuthal gamma-ray logs and the real-time gamma-ray log (raw and smoothed) within this window, and through comparison of the sequence of extreme points in the upper and lower azimuthal gamma-ray logs, it is determined that the bit is up-cutting in this window. Figure 10b presents the

matching result of Scheme A (trend-constrained DTW); the error between the predicted endpoint (green square) and the reference endpoint (blue triangle) in this window is 0.05 m. Figure 10c presents the matching result of Scheme D (unconstrained DTW); the predicted endpoint drifts significantly due to the global search, deviating from the reference endpoint by approximately 0.8 m in this window. Figure 10d presents the matching result of Scheme E (Euclidean distance); the predicted endpoint deviates from the reference endpoint by about 0.2 m in this window.

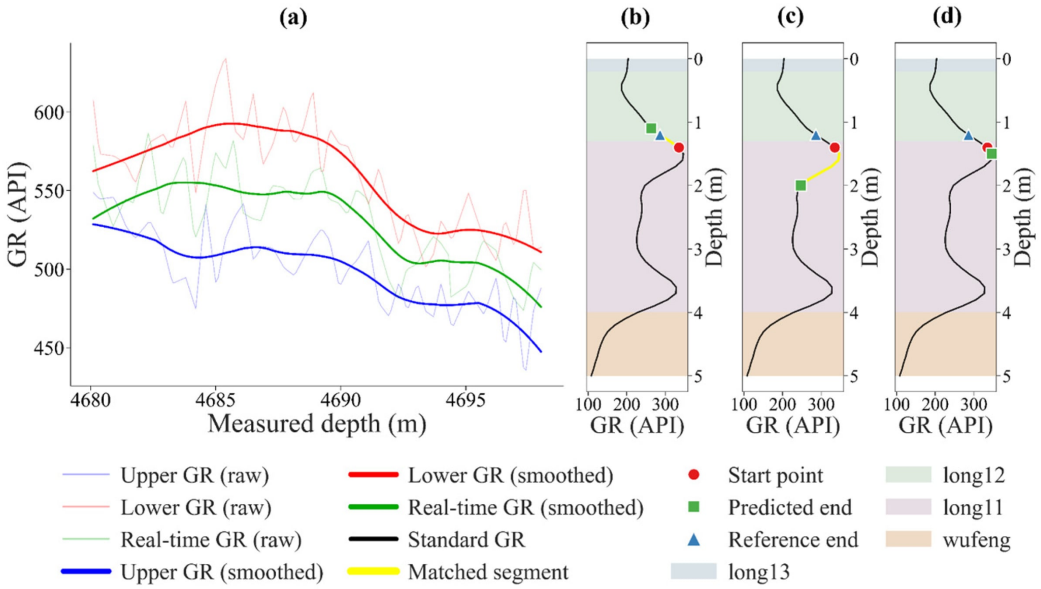

Figure 10. Comparison case of different matching schemes for the same geological window. (**a**) Upper and lower azimuthal gamma-ray logs and real-time gamma-ray log (raw and smoothed); (**b**) correct matching by Scheme A (trend-constrained DTW); (**c**) remote false matching by Scheme D (unconstrained DTW); (**d**) local shape mismatch by Scheme E (Euclidean distance).

The five schemes were run on test well H1; Figure 11 presents a comparison between the prediction results of each scheme and the field-interpreted reference, and Table 4 presents the corresponding quantitative metrics.

Table 4. Comparison of ablation experiment results.

Method	Similarity Metric	Trend Constraint	Adaptive Threshold	MAE (m)	Max Error (m)	Std (m)	MAE Reduction vs. D (%)
A	DTW	Yes	Yes	0.314	1.000	0.346	55.9%
B	DTW	Yes	No	0.360	1.000	0.353	49.4%
C	DTW	Yes	No	0.509	1.500	0.495	28.5%
D	DTW	No	No	0.712	2.000	0.619	Baseline
E	Euclidean	No	No	0.546	1.378	0.396	23.3%

As shown in Table 4, Scheme A (the full model) achieved the lowest mean positioning error across the 78 analysis windows in Well H1, with an MAE of 0.314 m, a maximum error of 1.000 m, and an error standard deviation of 0.346 m. The MAE of Scheme A was 55.9% lower than that of the unconstrained DTW baseline model D, and 12.8% lower than that of the fixed-threshold trend-constrained model B. The MAE of Scheme B was 0.360 m, a 49.4% reduction compared with Scheme D. Scheme C achieved an MAE of 0.509 m, higher than that of Scheme B. Scheme A further reduced the positioning error compared to Scheme B.

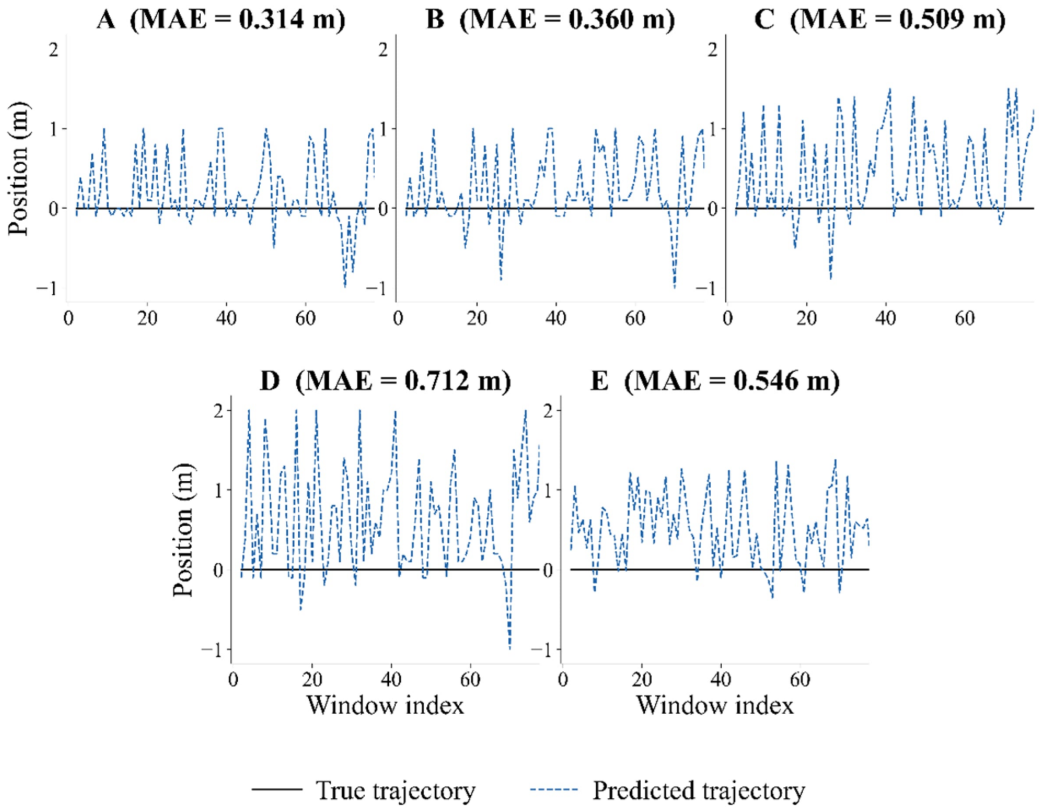

Figure 11. Comparison of window-level positioning results among different schemes.

To further analyze the error distribution and stability of the different methods across the 78 windows, Figure 12 presents the box plots and cumulative distribution functions (CDFs) of the window-level positioning errors for the five schemes (A–E). The box plots are used to compare the median error, dispersion, and outliers, while the CDFs are used to evaluate the window coverage proportion under different error thresholds.

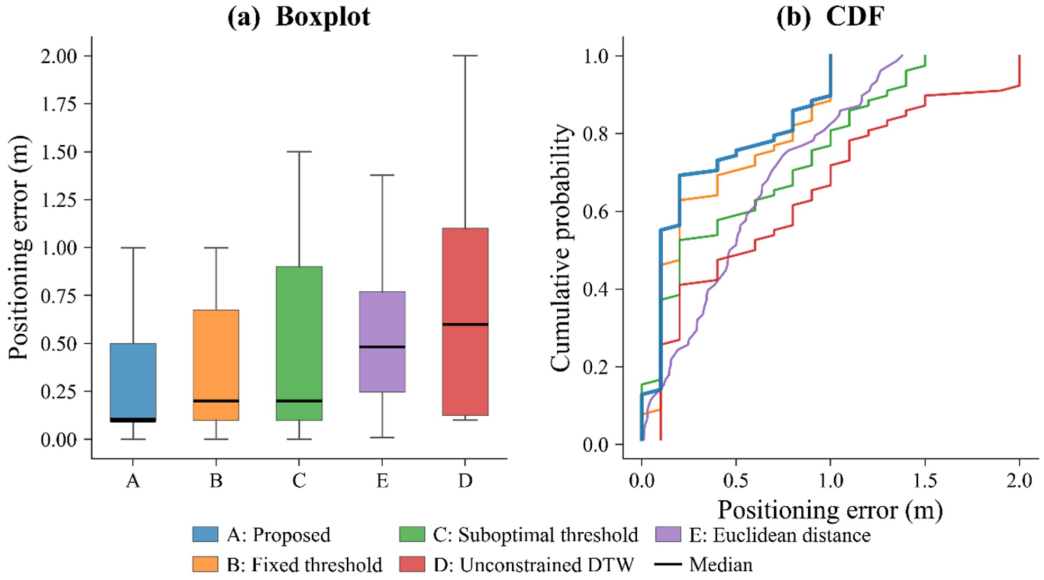

Figure 12. Boxplots and cumulative distribution functions (CDFs) of window-wise positioning errors for different schemes.

From the error distributions in Figure 12, the median error of Scheme A is comparable to that of Scheme B (both around 0.20 m), but its error dispersion (standard deviation

0.346 m) is the lowest among all schemes. Compared with Scheme D, the error distribution of Scheme B is shifted toward lower errors overall. The box and upper whisker of Scheme C are significantly expanded. The median error of Scheme E (Euclidean distance) is 0.482 m, higher than that of all trend-constrained DTW schemes (A, B, and C), and its error distribution is shifted to the right overall with larger dispersion. The CDFs further indicate that Scheme A consistently maintains the highest window coverage proportion under small error thresholds.

4.4. Independent Field Validation on Well H2

To further evaluate the reproducibility of the proposed method, an additional independent well, H2, was used for field validation. The same five comparison schemes (A–E) described in Section 4.2 were applied, and the positioning results are summarized in Table 5.

Table 5. Positioning performance of different matching schemes on independent Well H2.

Method	MAE (m)	Max Error (m)	Std (m)	MAE Reduction vs. D (%)
A	0.338	0.950	0.366	44.8%
B	0.392	1.130	0.412	36.0%
C	0.725	1.920	0.542	−18.5%
D	0.612	1.450	0.485	Baseline
E	0.491	1.540	0.458	19.8%

Scheme A achieved the lowest MAE of 0.338 m, with a maximum error of 0.950 m and an error standard deviation of 0.366 m. Under the same trend-constrained DTW framework, adaptive threshold updating reduced the MAE from 0.392 m (Scheme B) to 0.338 m (Scheme A), corresponding to a 13.8% improvement. This comparison isolates the contribution of the adaptive threshold module from that of the trend constraint. In addition, Scheme A exhibited a lower error standard deviation than Scheme B (0.366 m versus 0.412 m), suggesting reduced error dispersion in this independent test well. Compared with the unconstrained DTW baseline (Scheme D), Scheme A reduced the MAE by 44.8%, further demonstrating the overall benefit of combining directional constraints with adaptive threshold updating.

Scheme C exhibited the largest MAE of 0.725 m, exceeding that of the unconstrained DTW baseline. This result suggests that an improperly selected threshold may reduce the effectiveness of directional constraints and, in some cases, lead to greater positioning deviations than unconstrained matching. The performance differences among Schemes A–E are consistent with the importance of appropriate threshold selection and geological directional constraints in DTW-based positioning.

Across the two independent validation wells, the proposed method consistently outperformed the fixed-threshold trend-constrained DTW scheme, reducing MAE by 12.8% on H1 and 13.8% on H2. These results provide additional evidence that adaptive threshold updating can improve positioning agreement with field interpretations under different well-specific reference-log conditions within the same geological block. However, the current results do not establish the same level of performance across different basins or highly heterogeneous geological settings.

5. Discussion

5.1. Core Mechanism Analysis and Module Contributions

The comparison between Schemes B and D indicates that azimuthal trend constraints improve DTW positioning by restricting directionally inconsistent endpoint candidates.

Scheme E further indicates that pointwise Euclidean distance matching, without nonlinear warping or directional constraints, is less effective in handling local gamma-ray variations.

Scheme C demonstrates the sensitivity of trend-constrained matching to threshold selection. Compared with the fixed-threshold Scheme B, the adaptive Scheme A mainly reduces error dispersion and occasional large deviations (Figure 11), rather than uniformly improving every window.

The five-well LOWO results and independent H1/H2 tests support within-block transferability and an additional benefit from adaptive thresholds. However, these comparisons establish agreement with field-interpreted reference positions, not independently verified absolute geological accuracy.

The 20–40 m analysis windows follow field decision intervals with independently interpreted reference endpoints. Shorter windows may lack distinctive gamma-ray features, whereas longer windows may increase matching ambiguity. Because alternative window lengths lack independently interpreted endpoints, an optimal window length cannot be established from these data.

5.2. Application Conditions and Limitations of the Method

The method is intended for gamma-only geosteering where a representative standard type log, distinguishable gamma-ray signatures, and reliable azimuthal responses are available. It provides local endpoint positioning and auxiliary steering support, not autonomous trajectory control.

Key uncertainties arise from lateral mismatch between the standard log and the drilled formation, degraded azimuthal responses (e.g., borehole effects or thin interbeds), and the locally planar boundary approximation used in apparent-dip estimation. The latter depends on the independently interpreted start and predicted endpoint of the same window, together with wellbore geometry.

Geologically restricted endpoint searches and DTW matching cost can help flag questionable matches for manual review, but their effectiveness in detecting errors has not been quantitatively established. Because each window uses an independently interpreted start, the present implementation does not recursively propagate the preceding predicted endpoint; initial-anchor uncertainty remains a potential error source.

Relative to multi-parameter geosteering, the method requires fewer logging measurements but provides less geological information. It is therefore a complementary option for cost-sensitive wells rather than a substitute for integrated geological interpretation.

The proposed method employs a locally constrained DTW endpoint search, which limits the candidate matching range compared with an unrestricted search. However, computational latency has not been independently benchmarked, and real-time execution performance remains to be verified. In addition, no direct comparison with commercial geosteering software was conducted. The apparent dip estimates and steering recommendations are intended as auxiliary guidance and have not been independently validated against quantitative field benchmarks.

All seven wells are from the same block, so the evidence does not establish transferability to strongly heterogeneous formations or other basins. Reference endpoints are based on field interpretation and may contain uncertainty. Future work should test more diverse geological settings, independently verified benchmarks, initial-anchor perturbations, and sequential error-recovery strategies. Extending the current framework toward multi-sensor fusion and IoT-enabled real-time data pipelines [33] is also a promising direction for early detection of downhole anomalies during geosteering.

6. Conclusions

This study developed an azimuthal gamma-ray trend-constrained DTW framework with adaptive significance-threshold updating for in-zone positioning and auxiliary geosteering under limited logging conditions. The main conclusions are as follows:

(1) By incorporating the relative response order of upper and lower azimuthal gamma-ray measurements as a geological directional prior, the proposed method restricts DTW candidate endpoints according to the identified bit movement trend. This reduces directionally inconsistent matching and lowers the mean absolute positioning error by 55.9% and 44.8% on wells H1 and H2, respectively, compared with unconstrained DTW.

(2) An adaptive significance-threshold updating strategy based on window-level gamma-ray and matching features was developed. The XGBoost classifier selects a threshold category to accommodate inter-window variations in gamma-ray response. Compared with fixed-threshold trend-constrained DTW, this strategy further reduces the mean absolute error by 12.8% on H1 and 13.8% on H2, confirming the additional contribution of threshold adaptation beyond the trend constraint alone.

(3) Five-well leave-one-well-out cross-validation on 247 analysis windows achieved a macro-averaged MAE of 0.332 m, and independent validation on H1 and H2 yielded MAEs of 0.314 and 0.338 m, respectively. These results support within-block cross-well applicability. By combining endpoint positioning with local apparent dip estimation and auxiliary steering rules, the framework provides a quantitative and interpretable auxiliary reference for gamma-only geosteering, complementing rather than replacing multi-parameter interpretation or engineer judgment.

The main technical contribution is a lightweight, interpretable framework that injects an azimuthal gamma-ray directional prior into DTW matching and adapts its key threshold to window-level responses. Practically, it offers a low-cost auxiliary tool for in-zone positioning and steering support in gamma-only horizontal wells. However, the positioning errors are measured against field-interpreted reference positions, all validation wells are within the Da'an Block, and the dip estimates and steering recommendations have not been independently validated. Future work will address more heterogeneous formations, uncertainty in manually interpreted starting positions, computational performance, and comparison with commercial geosteering systems.

Author Contributions: Conceptualization, Z.Z. (Zexi Zhao); methodology, Z.Z. (Zexi Zhao), X.S. and G.Z.; software, Z.Z. (Zexi Zhao); validation, S.L., X.S., G.Z. and Z.Z. (Zhaobin Zhang); formal analysis, Z.Z. (Zexi Zhao), B.Z., G.Z. and H.H.; investigation, Z.Z. (Zexi Zhao), B.Z., X.S. and H.H.; resources, S.L., Z.Z. (Zhaobin Zhang) and X.L.; data curation, Z.Z. (Zexi Zhao), B.Z. and H.H.; writing—original draft preparation, Z.Z. (Zexi Zhao); writing—review and editing, S.L., X.S., Z.Z. (Zhaobin Zhang) and X.L.; visualization, Z.Z. (Zexi Zhao), B.Z. and G.Z.; supervision, S.L.; project administration, S.L.; funding acquisition, S.L. All authors have read and agreed to the published version of the manuscript.

Funding: This work was supported by the Key Research Program of the Institute of Geology & Geophysics, CAS (Grant No. PTYQ2026YZ0059).

Institutional Review Board Statement: Not applicable.

Informed Consent Statement: Not applicable.

Data Availability Statement: The datasets presented in this article are not readily available because the well data are proprietary and subject to confidentiality agreements with the data provider. Requests to access the datasets should be directed to the corresponding author and will be considered on a case-by-case basis, subject to permission from the data owner.

Acknowledgments: The authors gratefully acknowledge the technical support from the State Key Laboratory of Deep Petroleum Intelligent Exploration and Development, Institute of Geology and Geophysics, Chinese Academy of Sciences.

Conflicts of Interest: The authors declare no conflicts of interest. The funders had no role in the design of the study; in the collection, analyses, or interpretation of data; in the writing of the manuscript; or in the decision to publish the results.

Abbreviations

The following abbreviations/mathematical symbols/technical terms are used in this manuscript:

API	API gamma-ray unit
CDF	Cumulative distribution function
DTW	Dynamic time warping
GR	Gamma ray
LOWO	Leave-one-well-out cross-validation
LWD	Logging while drilling
MAE	Mean absolute endpoint positioning error relative to field-interpreted reference positions
MD	Measured depth along the wellbore
MWD	Measurement-While-Drilling
SEM	Standard error of the mean
TVD	True vertical depth
XGBoost	Extreme gradient boosting
Mathematical Symbols	
c_i	Threshold category of window i
$\hat{c}_i$	Predicted threshold category
$D(R_i, S_i)$	DTW distance between real-time and standard sequences
$\mathcal{D}$	Supervised dataset of feature vectors and threshold labels
D_1, D_2	Start and end wellbore points of an analysis window
d_i	Signed endpoint coordinate relative to target-zone top; $d_i = \hat{z}_i$
$f(\cdot)$	Classifier mapping window features to threshold category
H	Vertical target-zone thickness used for position classification
K	Number of threshold categories; four in this study
L_i	Window endpoint loss, described as absolute positioning error
$MAE(\lambda)$	Mean absolute endpoint error for the parameter setting evaluated
N	Number of analysis windows
P_i	Endpoint category: above, inside, or below the target zone
$Q(\cdot)$	Category-to-threshold lookup function
R_i	Real-time gamma-ray sequence in window i
$S(z)$	Standard type-log gamma-ray response at vertical coordinate z
$S_i(z_e)$	Standard log segment from the fixed starting anchor to candidate endpoint z_e
T_i	Trend category: up-cutting, down-cutting, or parallel/unknown
$\mathbf{x}_i$	Window state feature vector
$\hat{z}_i$	Predicted stratigraphic endpoint position of window i
z_i^{ref}	Field-interpreted reference endpoint position
$\hat{z}_{i-1}$	Independently field-interpreted starting anchor for the current window
z_e	Candidate endpoint position along the standard type log
α_2	Estimated local apparent formation dip over the window
δ	Boundary safety distance defining near-boundary regions
$\Delta h_1, \Delta h_2$	Vertical distances from the wellbore to the target-zone top at D_1 and D_2
Δh_d	Vertical change of the target-zone top: $\Delta TVD - (\Delta h_2 - \Delta h_1)$
Δl_d	Horizontal displacement between D_1 and D_2
ΔTVD	Change in wellbore true vertical depth over the window
$\Delta\theta_i$	Trajectory–formation angular difference $\theta_{b,i} - \hat{\theta}_{f,i}$
$\Delta z_{\max}$	Maximum vertical endpoint search distance from the starting anchor
$\theta_{b,i}$	Signed trajectory inclination in the profile plane, positive upward
$\hat{\theta}_{f,i}$	Estimated apparent formation dip used in Equation (13)
λ	Algorithm parameter varied in sensitivity analysis
λ_s	Significance threshold for insufficiently distinctive azimuthal responses
λ_i^*	Optimal historical-window threshold label; smallest threshold selected in a tie

$\hat{\lambda}_{s,i}$	Predicted threshold before temporal smoothing
$\lambda_{s,i}$	Smoothed threshold applied to window i
ρ	Exponential-smoothing coefficient, $0 \leq \rho \leq 1$
Ω_i	Trend-constrained candidate endpoint set
Technical Terms	
Analysis window	Measured-depth segment for local trend identification, matching, and positioning
Standard type log	Reference gamma-ray log providing a stratigraphic vertical coordinate
Fixed-start–sliding-end matching	Within-window matching with an independently interpreted start and searched endpoint
Apparent formation dip	Local dip in the trajectory profile plane
Macro-average	Arithmetic mean of well-level metrics with equal weight per well

References

1. Dahle, P.; Waade, B.S.; Almendral Vázquez, A.; Ohlsen, F. Geosteering: Continuous surface model updates using gamma log. In Proceedings of the SPE Annual Technical Conference and Exhibition, New Orleans, LA, USA, 28–30 September 2025. [CrossRef]
2. Du, H.; Dong, Y.; Hou, W.; Wang, C.; Sun, X.; Du, S.; Ye, Y. Application of integrated positioning, measurement, logging and guiding in improving the drilling rate of horizontal wells. *Geol. Surv. China* **2022**, *9*, 1–9. [CrossRef]
3. Lin, X.; Yuan, R.; Tan, W.; Xu, L.; Yang, L.; Li, Y. Formation-penetration identification method in azimuthal gamma geosteering based on dynamic time warping algorithm. *Pet. Drill. Tech.* **2026**, *54*, 23–30. [CrossRef]
4. Wang, G.; Jin, Z.; Liu, G.; Liu, Q.; Liu, Z.; Wang, H.; Liang, X.; Jiang, T.; Wang, R. Geological implications of gamma ray (GR) anomalies in marine shales: A case study of the Ordovician-Silurian Wufeng-Longmaxi succession in the Sichuan Basin and its periphery, Southwest China. *J. Asian Earth Sci.* **2020**, *199*, 104359. [CrossRef]
5. Gee, T.; Maus, S.; Mitkus, A.M.; McCarthy, K.; Velozzi, D.M.; Mottahedeh, R. Improving wellbore placement accuracy using stratigraphic misfit heatmaps. In Proceedings of the SPE/AAPG/SEG Asia Pacific Unconventional Resources Technology Conference, Brisbane, Australia, 3–5 December 2019. [CrossRef]
6. Kim, J. New geomechanical application utilizing MWD gamma ray logs: An Eagle Ford case study. *J. Pet. Sci. Eng.* **2021**, *196*, 108043. [CrossRef]
7. Jeong, C.; Lin, S.-H.; Reynier, A.; Gremillion, J.; Sharma, V.; Alshaikh, F.; Akpenyi, C. Automated gamma ray-based structural interpretation for optimized geosteering in a horizontal well. In Proceedings of the SPE/AAPG/SEG Unconventional Resources Technology Conference, Houston, TX, USA, 23–25 June 2025. [CrossRef]
8. Krygier, N.; Solarin, A.; Orozova-Bekkevold, I. A drilling company's perspective on non-productive time (NPT) due to well stability issues. In Proceedings of the SPE Norway Subsurface Conference, Virtual, 2–3 November 2020. [CrossRef]
9. Jiang, D.; Yuan, W.; Qi, B.; Yu, H.; Zhang, L. Current status and outlook of neutron logging-while-drilling technology. *Processes* **2026**, *14*, 1269. [CrossRef]
10. Zhao, A.; Yu, Y.; Wang, B.; Liu, Y.; Liu, J.; Fu, X.; Zheng, W.; Tian, F. Real-time intelligent recognition and precise drilling in strongly heterogeneous formations based on multi-parameter logging while drilling and drilling engineering. *Appl. Sci.* **2025**, *15*, 5536. [CrossRef]
11. Jahani, N.; Alyaev, S.; Ambía, J.; Fossum, K.; Suter, E.; Torres-Verdín, C. Enhancing the detectability of deep-sensing borehole electromagnetic instruments by joint inversion of multiple logs within a probabilistic geosteering workflow. *Petrophysics* **2023**, *64*, 80–91. [CrossRef]
12. Lu, B.; Ni, W. Key technologies of high-precision imaging logging while drilling. *Pet. Drill. Tech.* **2019**, *47*, 148–155. [CrossRef]
13. Cheng, G.; Qi, Z.; Wang, B.; Wu, Z. Application of near-bit azimuth gamma geosteering technology in Dongsheng gas field. *Mud Log. Eng.* **2023**, *34*, 79–84. [CrossRef]
14. Kang, Z.; Zhang, Y.; Qin, H.; Gan, W.; Chen, G. An intelligent inversion method for azimuth electromagnetic logging while drilling measurements. *IEEE Access* **2023**, *11*, 79285–79294. [CrossRef]
15. Wang, Z.; Xu, W.; Wang, W.; Liang, M.; He, J.; Qian, C.; Zou, H. Application of 3D geological modeling combined with gamma imaging technology in shale oil geosteering. *J. Xi'an Shiyou Univ. (Nat. Sci. Ed.)* **2024**, *39*, 112–119. [CrossRef]
16. Noaman, A.; Bin Zaqr, S.; Shohdy, A. Geosteering thin carbonate reservoirs by the near-bit gamma ray image (NBGR-Image). In Proceedings of the Middle East Oil, Gas and Geosciences Show (MEOS GEO), Manama, Bahrain, 16–18 September 2025. [CrossRef]
17. Zong, C.; Liu, J.; Liu, Z.; Liu, Y.; Wang, C.; Gao, H.; Duan, J.; Zhou, J. A fast forward algorithm of azimuthal gamma imaging logging while drilling. *Appl. Radiat. Isot.* **2023**, *194*, 110659. [CrossRef] [PubMed]

18. Lu, M.; Cai, D.; Fu, X.; Cheng, S.; Sun, Y.; Liu, P.; Jiao, Y. An intelligent log-seismic integrated stratigraphic correlation method based on wavelet frequency-division transform and dynamic time warping: A case study from the Lasaxing oilfield. *Energy Geosci.* **2025**, *6*, 100412. [CrossRef]
19. Sylvester, Z. Automated multi-well stratigraphic correlation and model building using relative geologic time. *Basin Res.* **2023**, *35*, 1961–1984. [CrossRef]
20. Kesireddy, V.; Gildin, E. Deep reinforcement learning and human-in-the-loop preference learning to address uncertainty in geosteering. Paper Presented at the IADC/SPE International Drilling Conference and Exhibition, Galveston, TX, USA, 17–19 March 2026. [CrossRef]
21. Yuan, C.; Zhou, C.; Zhang, F.; Hu, S.; Li, C. A novel method for quantitative geosteering using azimuthal gamma-ray logging. *Appl. Radiat. Isot.* **2015**, *96*, 63–70. [CrossRef] [PubMed]
22. Zhang, B.; Wen, H.; Qing, H.; Yang, K.; Luo, Y.; Yang, H.; Wang, P.; He, L.; Xiao, W. The influence of depositional and diagenetic processes on rock electrical properties: A case study of the Longmaxi Shale in the Sichuan Basin. *J. Pet. Sci. Eng.* **2022**, *211*, 110119. [CrossRef]
23. Zhou, X.; Zhao, J.; Yan, B.; Zhu, Z.; Yang, N.; Liang, P.; Guo, W. Deep-water traction current sedimentation in the Lower Silurian Longmaxi Formation siliceous shales, Weiyuan area, Sichuan Basin, China, using nano-resolution petrological evidence. *Minerals* **2025**, *15*, 723. [CrossRef]
24. Ma, X.; Xie, J.; Yong, R.; Zhu, Y. Geological characteristics and high production control factors of shale gas reservoirs in Silurian Longmaxi Formation, southern Sichuan Basin, SW China. *Pet. Explor. Dev.* **2020**, *47*, 841–855. [CrossRef]
25. Liang, F.; Zhao, Q.; Shi, X.; Wang, Y.; Zhang, Q.; Zhou, S.; Qi, L.; Cui, H. A new method for isochronous stratigraphic division of Longmaxi Formation in Sichuan Basin. *Acta Pet. Sin.* **2023**, *44*, 1274–1298. [CrossRef]
26. Qin, Z.; Pan, H.; Wang, Z.; Wang, B.; Huang, K.; Liu, S.; Li, G.; Amara Konaté, A.; Fang, S. A fast forward algorithm for real-time geosteering of azimuthal gamma-ray logging. *Appl. Radiat. Isot.* **2017**, *123*, 114–120. [CrossRef] [PubMed]
27. Ding, W.; Hou, S.; Tian, S.; Liang, S.; Liu, D. A Bayesian optimized variational mode decomposition-based denoising method for measurement while drilling signal of down-the-hole drilling. *IEEE Trans. Instrum. Meas.* **2023**, *72*, 1–14. [CrossRef]
28. Zhang, H.; Li, H.; Lu, D.; Xie, Y. An improved LWD azimuth gamma imaging model based on HSI space. *IEEE Access* **2020**, *8*, 112160–112169. [CrossRef]
29. Itakura, F. Minimum prediction residual principle applied to speech recognition. *IEEE Trans. Acoust. Speech Signal Process.* **1975**, *23*, 67–72. [CrossRef]
30. Sakoe, H.; Chiba, S. Dynamic programming algorithm optimization for spoken word recognition. *IEEE Trans. Acoust. Speech Signal Process.* **1978**, *26*, 43–49. [CrossRef]
31. Sun, Q.; Li, N.; Duan, Y.; Li, H.; Tang, H. Logging-while-drilling formation dip interpretation based on long short-term memory. *Pet. Explor. Dev.* **2021**, *48*, 843–850. [CrossRef]
32. Bai, J.; Wang, S.; Xu, Q.; Lai, K.; Xu, S.; Zhang, J.; Ju, Y.; He, Z. Adaptive threshold multimodal fusion for rock prediction in complex geological environments while drilling. *Bull. Eng. Geol. Environ.* **2025**, *84*, 178. [CrossRef]
33. Elmgerbi, A.; Thonhauser, G. *Assessing the Potential of Advanced Sensor Technologies and IoT in Predicting Downhole Drilling Issues*; GOTECH: Dubai, United Arab Emirates, 2025. [CrossRef]

Disclaimer/Publisher's Note: The statements, opinions and data contained in all publications are solely those of the individual author(s) and contributor(s) and not of MDPI and/or the editor(s). MDPI and/or the editor(s) disclaim responsibility for any injury to people or property resulting from any ideas, methods, instructions or products referred to in the content.